Article

# Ceramic-based Multi-Site Platinum Microelectrode Arrays: Morphological Characteristics and Electrochemical Performance for Extracellular Oxygen Measurements in Brain Tissue

Ana Ledo, Cátia F. Lourenço, João Laranjinha, Christopher M.A. Brett, Greg A. Gerhardt, and Rui M. Barbosa

*Anal. Chem.*, **Just Accepted Manuscript** • DOI: 10.1021/acs.analchem.6b03772 • Publication Date (Web): 12 Jan 2017

# Ceramic-based Multi-Site Platinum Microelectrode Arrays: Morphological Characteristics and Electrochemical Performance for Extracellular Oxygen Measurements in Brain Tissue

Ana Ledo[1], Cátia F. Lourenço[1], João Laranjinha[1,2], Christopher M. A. Brett[3], Greg A. Gerhardt[4] and Rui M. Barbosa[§,1,2]

[1] Center for Neuroscience and Cell Biology, University of Coimbra, Portugal

[2] Faculty of Pharmacy, University of Coimbra, Portugal

[3] Department of Chemistry, Faculty of Sciences and Technology, University of Coimbra, Coimbra, Portugal

[4]Center for Microelectrode Technology (CenMeT), Department of Neuroscience, University of Kentucky Medical Center, Lexington, USA

[§] Corresponding Author

Rui M. Barbosa
Faculty of Pharmacy
University of Coimbra
Health Sciences Campus
Azinhaga de Santa Comba
3000-548 Coimbra, Portugal

rbarbosa@ff.uc.pt

## Abstract

Ceramic-based multisite Pt microelectrode arrays (MEAs) were characterized for their basic electrochemical characteristics and used for *in vivo* measurements of oxygen with high resolution in the brain extracellular space. The microelectrode array sites showed a very smooth surface mainly composed of thin-film polycrystalline Pt, with some apparent nano-scale roughness that was not translated into an increased electrochemical active surface area. The electrochemical cyclic voltammetric behavior was characteristic of bulk Pt in both acidic and neutral media. In addition, complex plane impedance spectra showed the required low impedance (0.22 MΩ; 10.8 Ω $cm^2$) at 1 kHz) and very smooth electrode surfaces. The oxygen reduction reaction on the Pt surface proceeds as a single 4-electron reduction pathway at -0.6 V *vs* Ag/AgCl reference electrode. Cyclic voltammetry and amperometry demonstrate excellent electrocatalytic activity towards oxygen reduction in addition to a high sensitivity (-0.16 ± 0.02 nA $\mu M^{-1}$), and a low limit of detection (0.33 ± 0.20 μM). Thus, MEAs provide an excellent microelectrode platform for multi-site oxygen recording *in vivo* in the extracellular space of the brain, demonstrated in anaesthetized rats, and hold promise for future *in vivo* studies in animal models of CNS disease and dysfunction.


**Keywords**: Platinum Microelectrode Array; Oxygen Reduction; Brain Tissue Oxygen.

## Introduction

Monitoring brain oxygen levels *in vivo* has been used over the last decade in patients after brain injury resulting from ischemia, tissue hypoxia, trauma and stroke, among others, allowing the implementation of strategies to maintain adequate levels of tissue oxygen tension ($pO_2$) for improved treatment[1-3]. More recently**,** the ability to measure changes in $pO_2$ under conditions of large metabolic and hemodynamic responses such as those observed in epilepsy or traumatic brain injury has become increasingly important in understanding and managing these medical conditions[4].

Despite the need for *in vivo* measurement of $pO_2$, the complexity of the cerebral *milieu* has hindered the achievement of reliable measures. Quantitative measurements of $pO_2$ *in vivo* have been collected using a number of invasive and noninvasive methods such as i) fiber optic fluorescence ii) near-infrared spectroscopy iii), positron emission tomography (PET), iv) nuclear magnetic resonance (NMR), and v) electron paramagnetic resonance (EPR)[2,5-9].

The direct measurement of $O_2$ in brain tissue by electrochemical methods with microelectrodes allows for measurements of basal levels and changes of $pO_2$ with high spatial and temporal resolution. In this context, the Clark-type electrode (sensor) technology coupled with amperometry has, for many years, been considered the "gold standard" technique to directly monitor $pO_2$ [10]. Limitations of this approach include acute tissue damage, $O_2$ consumption by the probe, electrical noise, drift in calibration and slow response time[2,11].

A wide variety of microelectrodes has been used including noble metal electrodes such as Pt [10,12,13] and Au [14] as well as carbon-based electrodes (e.g. glassy carbon, carbon paste and carbon fibers)[15-17]. Platinum has excellent electrode properties for stimulation and recording in neuronal interfacing[18] and is recognizably the most active

metal towards the electrocatalytic reduction of $O_2$ facilitating the 4-electron reduction to $H_2O$ [19,20]. It is highly biocompatible and inert[21-23], allowing for long-term implantation of Pt-based devices with minimal corrosion-linked allergic reactions as observed with other metals such as Ni or Cu[18]. Furthermore, its high conductivity is ideal for the design of both stimulation and recording electrodes[18,24-26]. However, even on Pt-based materials the oxygen reduction reaction (ORR) suffers from sluggish kinetics and requires the use of a high overpotential[20,27].

Currently, there has been much interest in the development of multiplexed sensors for simultaneous measurements of metabolic markers (e.g. glucose, lactate and $O_2$) from multiple brain areas with high spatial and temporal resolution[27]. Advances in microfabrication technologies allow for the design of microelectrode array (MEA) platforms comprising multiple Pt sites arranged in a variety of configurations [28].

Ceramic-based multi-site Pt MEAs, designed and developed at the Center for Microelectrode Technology (CenMeT), University of Kentucky, USA, are fabricated using photolithographic techniques in well-defined and highly reproducible geometrical configurations. These MEAs have been extensively used for measuring tonic and rapid phasic changes in glutamate levels in anesthetized[29] and awake animals[30] as well as lactate[31] and glucose[32]. Interestingly, MEAs can also be configured for multi-analyte detection, as described for choline and acetylcholine[33]. Reports show that these MEAs maintain their recording capabilities during chronic measurements of neurotransmitters and multiple single-unit neuronal activity[34-36]. The use of a ceramic support material positively enhances the biocompatibility of these implantable MEAs, in addition to providing mechanical strength and electrical inertness[37,38].

Despite the versatility of the MEA platform, *in vivo* oxygen measurements in the brain of anesthetized or awake animals using these MEAs with high spatial and

temporal resolution have not been investigated to date. In the present work, we extend the previous morphological characterization of MEAs[37] and carried out a thorough electrochemical characterization of the latest formulations of these ceramic-based Pt multisite MEAs, which have been mass produced in the thousands, for *in vivo* recordings of $pO_2$ in the brain extracellular space. We evaluated the general electrochemical properties of the microelectrode arrays using cyclic voltammetry and electrochemical impedance spectroscopy. Finally, we demonstrate the ability of MEAs to record brain $pO_2$ in the extracellular space in anesthetized rats.

## Materials and Methods

### Reagents and Solutions

All reagents used were analytical grade and obtained from Sigma-Aldrich. Unless otherwise stated, all *in vitro* microelectrode evaluations were performed in PBS Lite 0.05 M pH 7.4 with the following composition: 10 mM $Na_2HPO_4$, 40 mM $NaH_2PO_4$, and 100 mM NaCl. For the electrochemical impedance evaluation, the PBS composition was as follows: 10 mM $Na_2HPO_4$, 40 mM $NaH_2PO_4$, and 100 mM $Na_2SO_4$. Saturated $O_2$ solutions for MEA calibration were prepared by bubbling PBS with 95% $O_2$ at 37 ºC for 20 min, resulting in an $O_2$ solution of 1.0 mM concentration[39].

### Ceramic-based Platinum Microelectrode Arrays

S2 type ceramic-based Pt MEAs were used, supplied by the Center for Microelectrode Technology (CenMet), University of Kentucky, USA), which are commercially available through the Center's website.

### Scanning Electron Microscopy and Elemental Composition Analysis

High-resolution scanning electron microscopy (SEM) was performed using a field emission scanning electron microscope coupled with energy dispersive X-ray spectroscopy (EDS) (Zeiss Merlin coupled to a GEMINI II column). The elemental composition was obtained from backscattered electron detection using EDS at 10 keV (Oxford Instruments X-Max). Conductive carbon adhesive tabs were used to ground the MEA surface and secure the sample on the specimen holder.

**Electrochemical Instrumentation**

Electrochemical characterization was performed on a Compactstat Potentiostat (Ivium, The Netherlands) using a three-electrode electrochemical cell comprising the MEA as working electrode, Ag/AgCl in 3M KCl as reference electrode (RE-5B, BAS Inc, IN, USA) and a Pt wire as auxiliary electrode. Amperometric MEA calibrations and recordings in anesthetized rats were performed using a FAST16mkIII potentiostat (Quanteon, KY, USA) in a two-electrode electrochemical cell configuration. For *in vivo* recordings, the Ag/AgCl in 3M KCl reference electrode was replaced by a miniature-reference electrode produced by electro-oxidation of the exposed tip of a Teflon-coated Ag wire (200 μm o.d., Science Products GmbH, Hofheim, Germany) in 1M HCl saturated with NaCl, which, when in contact with cerebrospinal fluid in the brain containing chloride ions, develops an Ag/AgCl half-cell.

**Microelectrode Calibration**

The S2 MEAs were routinely calibrated to assess performance. Calibrations were performed in 0.05 M PBS Lite pH 7.4 (20 mL) at 37 ºC with continuous stirring at low speed (240 rpm). Oxygen was removed by purging the solution with argon for a minimum period of 30 min, after which the needle was removed from solution and kept

above the surface to decrease $O_2$ back-diffusion to the calibration medium. Once a stable baseline was obtained, 4.95 μM aliquots of the $O_2$ saturated solution were added in 5 repetitions (concentration range 0-25 μM). The mean display frequency of the $O_2$ concentration was set at 4 Hz.

**Animals**

All the procedures used in this study were performed in accordance with the European Union Council Directive for the Care and Use of Laboratory animals, 2010/63/EU and were approved by the local ethics committee (ORBEA) and the Portuguese General Direction for Agriculture and Veterinary. One male Wistar rat weighing 300 g (Charles-River Laboratories) was used in these experiments. While in the animal facility, animal husbandry conditions were as follows: housed in pairs in filter-topped type III Makrolon cages in the local vivarium with controlled environmental conditions, including a temperature of 22-24 ºC, relative humidity of 45-65%, air exchange rate of 15 times per hour, 12 h light/dark cycle and with standard rat chow diet (4RF21-GLP Mucedola, SRL, Settimo Milanese, Italy) and chlorinated water available *ad libitum*.

***In vivo* recording of oxygen in the brain of anesthetized rats.**

The experimental setup used for amperometric monitoring of $O_2$ *in vivo* in anesthetized rats was similar to that used in previous studies[40]. Briefly, the animal was anesthetized with urethane 1.25 g/kg (i.p.) and placed in a stereotaxic apparatus. Body temperature was maintained at 37 ºC with a heated pad coupled to a Gaymar Heating Pump (Braintree Scientific, Inc., USA).

The skull was exposed by a midline scalp incision and retraction of the skin and temporal muscle. Bleeding was controlled using a Bovie® cautery. A craniotomy was made over the parietal cortex with an area of roughly 7 $mm^2$ (ML: +1 to +4 mm; AP: -2 to -5 mm relative to bregma) with removal of the overlying meninges. The S2 MEA was positioned in the parietal cortex so that the most proximal recording sites (3/4) were localized immediately below the brain surface. An additional small burr-hole was drilled in a site remote from the recording area for the insertion of a miniature Ag/AgCl reference electrode in the subdural space. The cortical surface was maintained wet with saline soaked cotton balls. After insertion of the MEA into the brain, the baseline was allowed to stabilize for at least 60 min. The mean display frequency was set at 100 Hz. Physiological parameters, namely arterial oxygen saturation, heart and breath rates were monitored using the MouseOx Plus pulse oximeter, with a recording frequency of 1 Hz (Starr Life Sciences Corp., PA, USA).

**Data Analysis**

Data analysis was performed using FAST Analysis version 6.0, OriginPro 2016 and GraphPad 5.0. Values are given as the mean ± coefficient of variation (%). The number of repetitions is indicated in each individual determination. Normality of data was confirmed using the D'Agostino & Pearson omnibus normality test ($\alpha$=0.05). Calculated parameters were statistically evaluated by using an unpaired two-tailed Student's t-test. Statistical significance was defined as $p<0.05$. The sensitivity of MEAs towards oxygen reduction was determined by linear regression analysis in the range 0-25 μM. The limit of detection (LOD) was defined as the concentration that corresponds to a signal-to-noise ratio of 3.

## Results and Discussion

### Characterization of the Pt surface

Platinum MEAs are patterned on 125 μm-thick ceramic wafers ($Al_2O_3$; Coors, Golden, CO) by means of photolithography and the interconnecting lines are insulated by a 1.5 μm layer of polyimide to protect against the high salt environment of the brain and physical cross-talk between recording sites. MEAs are fabricated in a well-defined geometrical configuration with high intra- and inter-electrode reproducibility. All MEAs used in this work had the S2 configuration, containing four 15 x 333 μm Pt sites distributed in two in-line pairs separated 100 μm between the edges of top and bottom pairs and 30 μm between side-by-side recording sites. The fabrication processes of the ceramic-based multi-site Pt microelectrode arrays have been previously described[41,42].

### Morphology and Chemical Analysis

Pt surfaces are of paramount importance in electrocatalysis[20] and other applications involving neural interfacing[43]. The elemental composition of the Pt recording site was analyzed using energy dispersive X-ray spectroscopy (EDS) performed on the outer surface of the Pt. As shown in Fig 1A, it was confirmed that the active site was mainly composed of Pt (95%) with several Pt peaks resulting from different electron orbitals being observed as well as the presence of a small proportion of C (5%). The presence of C may result from impurities present in the sputtering chamber, hydrocarbon contamination or even detection of C from the polyimide isolation layer or the conductive carbon adhesive tabs that were used to ground and secure the MEA to the specimen holder. Standard MEA cleaning procedures using 50% isopropanol often remove the carbon, which appears to be surface contamination from the sputtering chamber, since further analysis a few angstroms into the surface shows

that the Pt surface is > 99% Pt [37]. The Pt surface morphology of S2 MEAs is shown in the SEM micrographs of the planar surface and cross-section of the MEA in Fig. 1B-E. The polyimide layer closely surrounds each Pt pad without covering the recording sites and forms a microwell structure due to the recessed Pt recording pad (Fig. 1B). Despite the apparent surface smoothness (Fig. 1C), the recording sites show some surface irregularities with nanometer size elevations and depression of the surface, reported previously to have an absolute size below 5 nm[37]. The existence of a nanostructured surface has been demonstrated to improve MEA performance[44], possibly due to increased surface area. The cross-section images presented in Fig. 1E revealed a thin layer of the sputtered Pt, with a thickness of around 250 nm, which is in agreement with the specification for manufacturing of the MEAs.

**Electrochemically Active Surface Area**

Considering the nanostructured nature of the surface of the Pt recording site revealed by SEM analysis and the putative contribution of increased electroactive surface area for enhanced electrocatalytic performance, we determined the electrochemical active surface area (ECSA) of the Pt recording sites using two different approaches, as described below. Pt has the ability to undergo hydrogen underpotential deposition ($H_{upd}$), a characteristic that allows for the determination of the ECSA by measuring the hydrogen adsorption charge ($Q_H$)[45]. For this purpose, a cyclic voltammogram (CV) was recorded in $N_2$-saturated 0.5 M $H_2SO_4$ electrolyte solution and calculated for the negative-going scan after correction for pseudo-capacity in the double-layer region (Fig. 2A). This methodology assumes that the charge under the voltammetric peaks for hydrogen adsorption results from one hydrogen atom per Pt atom of the electrode surface. Using this approach and assuming that the formation of

the monolayer of hydrogen at a polycrystalline Pt surface requires 210 μC $cm^{-2}$ [46], the mean ECSA of the Pt sites on S2 MEAs was determined to be 5.28 x $10^{-5}$ $cm^2$ ± 29.7% ($n$=13), which corresponds to a surface roughness of 1.06 ± 29.8% ($n$=13). It is important to mention that staircase cyclic voltammetry is not appropriate for determining the correct charge in time-dependent processes such as proton adsorption[47], and thus the current averaging mode of cyclic voltammetry available in the Ivium Compactstat potentiostat was employed.

In the second approach, a standard electrochemical redox couple was used to determine the electrochemical behavior of the Pt MEA. Cyclic voltammetry was carried out in 5.0 mM hexammineruthenium(III) chloride ($Ru(III)(NH_3)_6$) in 0.5 M KCl solution at scan rates from 25 to 200 mV $s^{-1}$. As can be observed in Fig. 2B, the CVs revealed a hybrid behavior between conventional cyclic voltammetric and microelectrode behavior[48] with well-defined symmetrical oxidation and reduction peaks appearing already at 25 mV $s^{-1}$. In addition, both the anodic and cathodic peak currents ($I_{pa}$ and $I_{pc}$, respectively) varied linearly with the square root of the scan rate (Fig. 2C; $R^2$ values of 0.996 and 0.998, for $I_{pa}$ and $I_{pc}$, respectively) indicating that the process was diffusion-controlled. The average $I_{pa}/I_{pc}$ ratio was 0.89 ($n$=16), which is close to the theoretical value of 1 for a totally reversible reaction. The mean difference in quartile potentials, $|E_{1/4}-E_{3/4}|$ was 53.8 mV at 25 mV $s^{-1}$ and did not vary with scan rate, indicating that the reaction is reversible when considering the Tomes criterion of 56.4 mV for a one-electron reversible reaction[49].

The electrochemically active surface area of the Pt sites of the MEA was estimated using the Randles-Sevick equation for a reversible oxidation-reduction reaction considering a diffusion coefficient of $D$ = 7.1x$10^{-6}$ $cm^2$ $s^{-1}$ [50]. The calculated

surface area of the Pt sites was $4.48 \times 10^{-5}$ $cm^2$ ± 22.7%, corresponding to a surface roughness of 0.90 ± 22.4% (*n*=16 sites).

As highlighted in Fig. 2C, both methodologies used to determine the ECSA of the Pt sites on the S2 MEA showed that, despite the nanostructured surface suggested by the SEM micrographs, the ECSA is approximately identical to the geometric area. This is a unique property of the Pt-based MEAs and can be attributed to the roughness features being only at the nanoscale level so that the behavior is that of a very smooth electrode.

In order to examine the effects of pre-conditioning, different electrochemical cleaning strategies were evaluated. Repeated cycling between -0.6 V and +0.4 V (50 cycles), anodic or cathodic pre-treatment (holding the potential at +1.2 V or -0.6 V *vs* Ag/AgCl, respectively) produced no significant changes in the CV profiles, only slight changes in $I_{pa}$ and $I_{pc}$. Furthermore, the ESCA determined after anodic pre-treatment showed similar values as with no pre-treatment. This result indicates little to no carbon contamination of the electrode surface. Interestingly, the increased surface roughness of Pt stimulation microelectrodes has been shown to increase Pt electrode performance, namely by decreasing impedance and increasing the current density and charge injection[51,52]. However, the existence of a smooth surface may be advantageous in impeding the occurrence of undesirable side reactions at the surface such as the reduction or oxidation of the solvent, supporting electrolyte, electrode material, or impurities[49].

**Electrochemical Behavior in Acidic Electrolyte and in neutral PBS**

The well-known characteristic cyclic voltammogram of Pt in acid solution was used to further examine the electrochemical behavior of the MEA. The S2 MEA was

characterized by cyclic voltammetry in $N_2$-flushed $H_2SO_4$ (0.5 M). Fig. 3A shows cyclic voltammograms recorded between -0.25 and 1.2 V *vs* Ag/AgCl at increasing scan rates (50-1000 mV $s^{-1}$) of a single Pt site of a S2 MEA. The typical CV exhibited redox peaks at -0.06 and -0.17 V, which could be attributed to strong and weak proton adsorption on Pt surfaces with (100) and (110) basal planes, respectively[53,54]. Furthermore, the presence of the three distinct peaks for $H^+$ desorption indicate a high quality Pt surface[54,55]. An oxidation wave is observed for $E > 0.5$ V due to the formation of Pt-O and Pt-OH oxide species on the Pt surface and there is a strong reduction peak at ca. 0.52 V corresponding to oxide reduction.

Although the CV plots obtained in acid electrolyte are of invaluable importance for the evaluation of the Pt surface properties, it is important to characterize the electrode behavior in a neutral physiological-like media such as 0.05 M PBS Lite at pH 7.4, which simulates brain extracellular fluid. As shown in Fig. 3B, the general CV profile was similar in both acid and neutral electrolyte. The expected negative shift in hydrogen adsorption/desorption and Pt-O formation/reduction peaks was accompanied by a decrease in peak current with increasing pH. Furthermore, the amplitude of the potential window remained the same (approx. 1.6 V). An increase in the aqueous solution potential window in buffered neutral electrolyte compared to acidic electrolyte has been described for nanostructured Pt surfaces[54], and the fact that we did not observe the same pH dependent effect is probably due to the overall smoothness of the Pt recording sites of the S2 MEAs.

**Electrochemical Impedance Spectroscopy**

Electrochemical impedance spectroscopy (EIS) is a powerful tool in the study of the physical and interfacial properties of electrochemical systems, so the impedance

characteristics of the Pt MEA were investigated. Spectra were recorded in $N_2$-flushed PBS Lite pH 7.4 at room temperature by applying a sinusoidal wave of amplitude 10 mV between 100 kHz and 0.1 Hz (10 frequencies per decade) at the OCP (+0.332 V *vs* Ag/AgCl). Prior to recording each spectrum, the electrode was held at this applied potential for 5 minutes.

The Bode plot obtained from the data is presented in Fig. 4A. The data were fitted to a Randles circuit[56] (see inset of Fig. 4B) consisting of the cell resistance in series with a combination of a constant phase element (CPE) in parallel with the series combination of a charge transfer resistance ($R_e$) and a Warburg impedance element ($W$). The latter accounts for mass transfer limitations imposed by diffusion, which appear at lower frequencies. The values for the charge transfer resistance, Warburg element and double layer capacitance from fitting to the equivalent electrical circuit are presented in Table 1.

The characteristics of the interface between the neural tissue and implanted electrodes are critical. Low impedance and high stability are desirable characteristics of chronically implanted electrodes, since a low impedance guarantees a higher efficiency because less energy is required to pass current to the tissue[24,51]. Besides use as amperometric sensors, metal electrodes such as this Pt microelectrode array are widely employed in biomedical applications for rapid multiple single-unit recordings and putatively as neural stimulating electrodes[24,57]. They present advantages over glass-encased microelectrodes, such as low impedance at high frequencies. Whilst decreasing the electrode size is highly desirable in order to ensure high spatial resolution of either recording or stimulation, this is accompanied by an increase in the interfacial impedance. The value of $Z'$ at 1 kHz is typically reported for impedance measurements on microelectrodes. In this work, the MEAs showed a $Z'$ value of 10.8 Ω $cm^2$ (0.217

MΩ before area normalization) at 1 kHz. These values are in line with those reported for bulk Pt (5.57 Ω $cm^2$)[58] and much higher than those reported for Pt surfaces with increased roughness resulting from deposition of Pt-black (1.12 x $10^{-9}$ Ω $cm^2$)[59] or conducting polymers such as PEDOT [52]. In an initial paper characterizing this type of ceramic based Pt MEA, Burmeister *et al*., reported a *Z*′ value of 17.8 ± 2.8 MΩ (445 Ω $cm^2$) at 500 Hz[41]. At 500 Hz, these newer generation MEAs show a significantly lower impedance value of 0.413 MΩ (20.6 Ω $cm^2$)[41], which suggests improved surface characteristics of the new design, better surface cleaning of the Pt during manufacturing and probably less contamination from surface carbon (unpublished data). The CPE exponent is very close to unity, which demonstrates that the Pt surface of the S2 MEA is very smooth, in agreement with the evidence from both the SEM micrographs and the determination of the ECSA.

**Oxygen Reduction Reaction at the Pt Surface**

The oxygen reduction reaction (ORR) has been extensively studied in the context of fuel cell development[60,61]. In general, the ORR follows one of two reaction pathways: direct 4-electron reduction (reaction 1) or a 2-step 2-electron reduction, with the generation of $H_2O_2$ as an intermediate that is further reduced to water (reactions 2 and 3).

$$\boldsymbol{O_2 + 4H^+ + 4e^- \rightarrow 2H_2O,\ E^o = 1.23\ V} \quad (1)$$

$$\boldsymbol{O_2 + 2H^+ + 2e^- \rightarrow 2H_2O_2,\ E^o = 0.67\ V} \quad (2)$$

$$\boldsymbol{H_2O_2 + 2H^+ + 2e^- \rightarrow 2H_2O,\ E^o = 1.76\ V} \quad (3)$$

Notwithstanding, little is still understood about electrode kinetics and electrocatalytic properties in physiologically relevant *milieu* regarding pH, temperature and ionic strength. A better understanding of electrode performance is critical to design improved strategies for long-term stability and performance *in vivo.*

Representative cyclic voltammograms in $N_2$–flushed and air-saturated (0.27 mM $O_2$) PBS Lite recorded at 100 mV $s^{-1}$ are shown in Fig. 5A. The diffusion-limited current for oxygen reduction is reached at ca. -0.2 V; at -0.45 V proton adsorption begins to predominate. Figure 5B shows a plot of the amperometric current measured at different applied potentials in $N_2$ saturated and air-saturated medium (0.27 mM $O_2$). The subtracted current (inset) indicates an extended plateau region down to -0.6 V *v*s Ag/AgCl.

Since the voltammograms show only one reduction step, it can be inferred that the ORR occurring at the Pt surface of these S2 MEAs appears to be a one-step 4-electron reduction reaction to $H_2O$, as expected from what has been previously described for the Pt surface[19].

To further establish the most suitable working potential for monitoring $O_2$ *in vivo*, calibrations were performed at applied potentials ranging from -0.1 to -0.8 V *vs* Ag/AgCl and both the sensitivity (slope) and LOD were determined. As shown in Fig. 5C, between -0.1 and -0.5 V *vs* Ag/AgCl, the sensitivity *vs* potential plot shows an increase in sensitivity reaching a plateau between -0.5 and -0.7 V. The LOD decreases from -0.1 to -0.6 V, and at more negative potentials has a constant value of ca. 0.3 µM. Considering both the plots in Fig. 5 panels A-C and the CV plot in $N_2$-flushed PBS in Fig. 3B, it is clearly observable that -0.7 V is already in the hydrogen evolution region and at the negative limit of the applied potential window in PBS Lite. Thus, the optimal working potential for monitoring $O_2$ was chosen to be -0.6 V *vs* Ag/AgCl. Fig. 5D

shows a representative calibration of an S2 MEA at a holding potential of -0.6 V *vs* Ag/AgCl as well as the respective calibration curves for each of the 4 sites of the S2 MEA (inset). Also highlighted in the top left corner of Fig. 5D is the rapid response of the 4 channels to the first addition of $O_2$. Thus, despite the slow stirring of the calibration media, one can still observe a rapid response towards oxygen reduction.

On average, the Pt MEAs exhibited an oxygen sensitivity of -0.16 nA $\mu M^{-1}$ ± 17.7% ($R^2$=0.98 ± 1.87%), a sensitivity/unit area of 3.2 mA $mM^{-1}$ $cm^{-2}$ ± 17.7 % and a LOD of 0.33 µM ± 67.6% (*n*=15). The analytical parameters determined by amperometry at an applied potential of -0.6 V vs. Ag/AgCl are summarized in Table 2, and are compared with those reported in the literature. As shown in Table 2, both the sensitivity and the LOD are in good agreement with those reported both for Pt-based microelectrodes, and also for carbon-based microelectrodes. The sensitivity was found to be one order of magnitude higher than that reported for similar thin-film Pt microelectrode arrays[62] or carbon epoxy microelectrodes[63] and similar to that reported for carbon paste microelectrodes[15] and for Pt/Ir disk microelectrodes[64]. The LOD is an analytical parameter that is either omitted or not determined in many publications. Although the value reported here (0.33 µM ± 67.5%) is slightly higher than that reported by others[64], it must be emphasized that the LOD is highly dependent on the experimental conditions in which the calibrations are performed. Here the oxygen amperometric response of the MEAs was assessed with minimum stirring, since it was previously reported that the oxygen electrode response in brain tissue was independent of flow[15]. Due to the MEA size and design it was not possible to perform calibrations in a closed vessel. However, increased stirring increased $O_2$ back-diffusion into the PBS Lite following $N_2$-flushing, leading to greater signal noise (thus negatively impacting

LOD, which is calculated as 3xSD of the baseline) while producing a positive drift in the recorded current.

The analytical parameters determined by amperometry at a holding potential of -0.6 V *vs* Ag/AgCl are summarized in Table 2.

**In vivo recording of changes in $pO_2$ in the anesthetized rat brain**

For *in vivo* recording in brain tissue, be it in the anesthetized or in the awake freely-moving rodent, high temporal and spatial resolutions are highly desirable with minimal tissue damage. This may be achieved with commercially available modified Clark-type microelectrodes[65-67], bare carbon fiber microelectrodes[17,68,69] and carbon paste microelectrodes[15]. To enhance the electrochemical characteristics of carbon fiber microelectrodes, others have carried out surface modifications with carbon nanotubes and/or electrodeposition of Pt[70]. However, these electrodes allow single-site recordings. The ability to record local $pO_2$ from multiple sites within the brain can be achieved with multisite Pt-MEAs with distinct pad geometries. Ultimately, recording using multisite biomorphic MEA designs (sites placed at specific distances to target specific brain regions) is possible[35,71].

In order to demonstrate the capability of the S2 MEA to monitor changes in oxygen *in vivo* in the rat brain, we monitored changes in the local $pO_2$ in the cerebral cortex of an anesthetized rat respiring air, $O_2$ and argon. As shown in Fig. 6, changing the $pO_2$ in the respired air produced changes in arterial blood $O_2$ saturation (bottom trace, in blue) that were accompanied by similar changes in local $pO_2$. For simplicity, only 2 channels are shown, one from each side-by-side pair of the MEA. The higher basal $pO_2$ recorded from the site closest to the surface is most likely a result of $O_2$ diffusion from the surrounding atmosphere in the exposed tissue.

## Conclusions

Ceramic-based multisite Pt MEAs were used for measurements of oxygen *in vitro* and *in vivo* in the brain extracellular space with high temporal and spatial resolution. The microelectrode array sites showed a very smooth surface mainly composed of a thin-film polycrystalline Pt (95%). The apparent nano-scale roughness of the Pt surface does not lead to an increased electrochemically active surface area, but the active surface area is proportional to the geometric area of the Pt surface. This is a unique feature of the MEAs that is often not seen for other microelectrodes.

Investigation of the electrochemical behavior of the Pt MEAs by cyclic voltammetry shows the characteristics of bulk Pt in acidic and neutral media. In addition, complex plane impedance spectra showed the necessary low impedance values ((0.22 MΩ; 10.8 Ω $cm^2$) at 1 kHz) and that the electrode surfaces are very smooth. The oxygen reduction reaction on the Pt surface proceeds as a 4-electron reduction pathway at -0.6 V *vs* Ag/AgCl. Electrochemical evaluation by cyclic voltammetry and amperometry evidences an excellent electrocatalytic activity towards oxygen reduction in addition to a high sensitivity (-0.16 ± 0.02 nA $\mu M^{-1}$), and a low limit of detection (0.33 ± 0.20 μM). Thus, MEAs provide an excellent microelectrode platform for multi-site oxygen recording *in vivo* in the extracellular space of the brain.

**Acknowledgements**

This work is funded by FEDER funds through the Operational Program Competitiveness Factors - COMPETE and national funds by FCT - Foundation for Science and Technology under the strategic project UID/NEU/04539/2013. C.F.L. acknowledges fellowship SFRH/BPD/82436/2011 from FCT. We acknowledge Quanteon, LLC for salary support of A.L.

**Conflict of interest**

G.A.G. is the sole proprietor of Quanteon, LLC, which makes the Fast16 recording system used for control of the MEA technology.

## Tables

**Table 1** – Summary of fitted parameter results for impedance spectroscopy measurements for the Pt MEAs. Values shown with * are normalized by surface area.

| *E* (V) | $R_s$ (kΩ) | $R_c$ (MΩ) <br> $*R_c$ (kΩ cm$^2$) | CPE, nF s$^{n-1}$ <br> *CPE (µF cm$^{-2}$ s$^{n-1}$) | n | *W* (x10$^6$) <br> (1/Ω s$^{-0.5}$) |
|---|---|---|---|---|---|
| +0.332 <br> (OCP) | 3.5 | 16.0 <br> *0.8 | 1.2 <br> *24.02 | 0.99897 | 0.7 |

**Table 2** – Analytical performance comparison of different microelectrodes towards the oxygen response *in vitro*. Data are presented as mean ± SD.

| Microelectrode Type | Sensitivity (nA µM$^{-1}$) | Linearity ($R^2$) | Sensitivity/unit area (mA.mM$^{-1}$.cm$^{-2}$) | LOD (µM) | References |
|---|---|---|---|---|---|
| Thin film Pt MEA (*n*=12) | -0.16 ± 0.02 | 0.98±0.02 | -3.2 ± 0.5 | 0.33 ± 0.2 | Current study |
| Thin film Pt MEA [b] (*n*=5) | -0.58 +/- 0.001[a] | nd | -0.735+/- 0.013 | nd | [59] |
| Pt/Ir disk (*n*=4-18) | -1.43 +/- 0.05 | 0.979 | -9.1 +/- 0.6 | 0.08 +/- 0.01 | [61] |
| Carbon paste disk (CPE) (*n*=4-16) | -1.09 ± 0.03 | 0.998±0.01 | -4.8 +/- 0.2 | 0.09 +/- 0.01 | [61] |
| Pt/VACNT-CF[c] | -0.91 | 0.995 | nd | nd | [62] |
| Pt/FCNA modified GCE [d] | nd | nd | -4.1 | nd | [63] |
| Carbon Epoxy (*n*=6) | -0.222 ± 0.017 | 0.992 | -0.148 +/ 0.011 a | <5 | [60] |
| OMC-TTF [e] | -30 | 0.995 | -5 [a] | 0.39 | [64] |

[a] calculated from data in publication
[b] chronoamperometry
[c] Platinized vertically aligned carbon nanotube (VACNT)-sheathed carbon fibers
[d] Pt-dispersed flower-like carbon nanosheet
[e] ordered mesoporous carbon functionalized with tetrathiafulvalene
[nd] not determined

## Figure Legends

**Figure 1** – Morphological and chemical analysis of the ceramic-based MEA Pt surface. A) Elemental composition of a Pt site of the S2 MEA obtained by SEM/EDX elemental analysis at 10 keV. B) SEM micrograph image of the top pair of Pt sites at the MEA tip, showing the polyimide insulation layer and the ceramic subtract and C) high magnification view of the smooth Pt surface. D) Cross-section SEM micrographs of the Pt layer over the ceramic substrate wafer showing nano-size elevations of Pt surface and E) the reduced thickness of the thin Pt film.

**Figure 2** - Determination of the electrochemically active surface area (ECSA) of the Pt sites on the MEAs. A) Representative cyclic voltammogram ($25^{th}$ scan) in $N_2$ saturated 0.5 M $H_2SO_4$ of a Pt MEA surface. Shaded area ($Q_H$) represents section used to determine the hydrogen adsorption ($H_{upd}$) charge. B) Cyclic voltammograms recorded in 5.0 mM $Ru(III)(NH_3)_6$ in 0.5 M KCl at scan rates ($\upsilon$) of 25, 50, 100, 150 and 200 mV $s^{-1}$ for a Pt surface and the inset is the plot of anodic ($I_{pa}$) and cathodic ($I_{pc}$) peak currents as a function of $\upsilon^{1/2}$ showing the respective slope (m) ± SE. C) The bar graph shows the mean roughness factor ($\rho$) of the Pt sites determined by each method. Values represent mean ± SD. Dashed line highlights $\rho$=1, where the ECSA equals the geometric area.

**Figure 3** – Electrochemical behavior in acidic and neutral electrolyte media. A) Successive cyclic voltammograms ($25^{th}$ scan) at increasing scan rates (50-1000 mV $s^{-1}$) obtained in $N_2$ saturated 0.5 M $H_2SO_4$, detailing the typical Pt oxide formation and reduction, proton adsorption (2 peaks) and reduction (3 peaks) and double layer zones. B) Comparative CV plots (0.2 V $s^{-1}$) recorded in $N_2$-saturated 0.05 M PBS, pH 7.4 (black line) and $N_2$-saturated 0.5 M $H_2SO_4$, pH 0.72 (red line) highlighting the positive shift in hydrogen evolution potential and increasing currents for Pt-oxide formation and reduction at lower pH on the Pt surface of the MEAs.

**Figure 4** – Electrochemical impedance spectroscopy measurements. A) Impedance-frequency plot (Bode plot) at the open circuit potential (OCP) of +0.332V *vs* Ag/AgCl

of an MEA Pt site. Filled squares represent |*Z*| values and open squares are those obtained for the phase shift. The open red square highlights the |Z| value at 1 kHz. B) Complex plane electrochemical impedance spectrum (Nyquist plot) of experimental data (open squares) for the MEAs. Red line shows fitting to the electrical equivalent circuit shown in the inset. $R_s$ solution resistance, $R_e$ electron or charge transfer resistance, *W* Warburg impedance element, and CPE constant phase element.

**Figure 5** – Electrochemical behavior of oxygen reduction at the Pt MEA surface. A) Cyclic voltammograms recorded at 100 mV $s^{-1}$ and B) amperometric current as a function of the applied potential in PBS in the absence ($N_2$ saturated) (grey line) and presence of $O_2$ (blue line) (air-saturated) in the solution. The inset in B) displays the subtracted current response. C) Sensitivity and LOD data obtained at different reduction potentials at 37 ºC for the Pt surface of the MEA. D). Plot shows a representative 4-channel calibration obtained at -0.6 V *vs* Ag/AgCl and the calibration curve for each channel (inset) of an MEA. Highlighted in the top left corner is the response of the 4 channels to the first addition of $O_2$ solution, showing fast response despite slow stirring of solution. Data in B) and C) represent mean ± SD. The SD bars are presented only in one direction for graphical simplicity.

**Figure 6** – Oxygen measurement *in vivo* in the brain of an anesthetized rat. Amperometric recording obtained from a MEA implanted in the rat cerebral cortex. Increase and decrease in local $pO_2$ as a result of having the animal breath $O_2$ saturated air (blue box) or Ar saturated air (red box). Top panel shows amperometric response from 2 sites while the lower panel shows changes in systemic $O_2$ saturation (blue line) and breath rate (grey line).

## References


(1) De Georgia, M. A. *J. Intensive Care Med.* **2015**, *30*, 473-483.
(2) Ndubuizu, O.; LaManna, J. C. *Antioxid. Redox Signaling* **2007**, *9*, 1207-1219.
(3) Nemani, V. M.; Manley, G. T. *Op. Techn. Neurosurg.* **2004**, *7*, 2-9.
(4) Ivanov, A. I.; Bernard, C.; Turner, D. A. *Neurobiol. Dis.* **2015**, *75*, 1-14.
(5) Mintun, M. A.; Lundstrom, B. N.; Snyder, A. Z.; Vlassenko, A. G.; Shulman, G. L.; Raichle, M. E. *Proc. Natl. Acad. Sci. U. S. A.* **2001**, *98*, 6859-6864.
(6) Osharina, V.; Ponchel, E.; Aarabi, A.; Grebe, R.; Wallois, F. *NeuroImage* **2010**, *50*, 600-607.
(7) Hyder, F.; Rothman, D. L.; Shulman, R. G. *Proc. Natl. Acad. Sci. U. S. A.* **2002**, *99*, 10771-10776.
(8) Ances, B. M. *J. Cereb. Blood Flow Metab.* **2004**, *24*, 1-6.
(9) Khan, N.; Williams, B. B.; Hou, H.; Li, H.; Swartz, H. M. *Antioxid. Redox Signaling* **2007**, *9*, 1169-1182.
(10) Jobst, G.; Urban, G.; Jachimowicz, A.; Kohl, F.; Tilado, O.; Lettenbichler, I.; Nauer, G. *Biosens. Bioelectron.* **1993**, *8*, 123-128.
(11) Springett, R.; Swartz, H. M. *Antioxid. Redox Signaling* **2007**, *9*, 1295-1301.
(12) Pletcher, D.; Sotiropoulos, S. *J. Electroanal. Chem.* **1993**, *356*, 109-119.
(13) Ward, W. K.; Wood, M. D.; Slobodzian, E. P. *J. Med. Eng. Technol.* **2002**, *26*, 158-167.
(14) Holmstrom, N.; Nilsson, P.; Carlsten, J.; Bowald, S. *Biosens. Bioelectron.* **1998**, *13*, 1287-1295.
(15) Bolger, F. B.; McHugh, S. B.; Bennett, R.; Li, J.; Ishiwari, K.; Francois, J.; Conway, M. W.; Gilmour, G.; Bannerman, D. M.; Fillenz, M.; Tricklebank, M.; Lowry, J. P. *J. Neurosci. Methods* **2011**, *195*, 135-142.
(16) Lowry, J. P.; Boutelle, M. G.; O'Neill, R. D.; Fillenz, M. *Analyst* **1996**, *121*, 761-766.
(17) Venton, B. J.; Michael, D. J.; Wightman, R. M. *J. Neurochem.* **2003**, *84*, 373-381.
(18) Cowley, A.; Woodward, B. *Platinum Met. Rev.* **2011**, *55*, 98-107.
(19) Yeager, E. *Electrochim. Acta* **1984**, *29*, 1527-1537.
(20) Wu, J.; Yang, H. *Acc. Chem. Res.* **2013**, *46*, 1848-1857.
(21) Geninatti, T.; Bruno, G.; Barile, B.; Hood, R. L.; Farina, M.; Schmulen, J.; Canavese, G.; Grattoni, A. *Biomed. Microdevices* **2015**, *17*, 24.
(22) Turner, N.; Armitage, M.; Butler, R.; Ireland, G. *Cell Biol. Int.* **2004**, *28*, 541-547.
(23) Pennisi, C. P.; Sevcencu, C.; Dolatshahi-Pirouz, A.; Foss, M.; Hansen, J. L.; Larsen, A. N.; Zachar, V.; Besenbacher, F.; Yoshida, K. *Nanotechnology* **2009**, *20*, 385103.
(24) Merrill, D. R.; Bikson, M.; Jefferys, J. G. *J. Neurosci. Methods* **2005**, *141*, 171-198.
(25) Jorfi, M.; Skousen, J. L.; Weder, C.; Capadona, J. R. *J. Neural Eng.* **2015**, *12*, 011001.
(26) Kozai, T. D.; Jaquins-Gerstl, A. S.; Vazquez, A. L.; Michael, A. C.; Cui, X. T. *ACS Chem. Neurosci.* **2015**, *6*, 48-67.
(27) Norskov, J. K.; Rossmeisl, J.; Logadottir, A.; Lindqvist, L.; Kitchin, J. R.; Bligaard, T.; Jonsson, H. *J. Phys. Chem. B* **2004**, *108*, 17886-17892.
(28) Weltin, A.; Kieninger, J.; Enderle, B.; Gellner, A. K.; Fritsch, B.; Urban, G. A. *Biosens. Bioelectron.* **2014**, *61*, 192-199.

(29) Mattinson, C. E.; Burmeister, J. J.; Quintero, J. E.; Pomerleau, F.; Huettl, P.; Gerhardt, G. A. *J. Neurosci. Methods* **2011**, *202*, 199-208.
(30) Rutherford, E. C.; Pomerleau, F.; Huettl, P.; Stromberg, I.; Gerhardt, G. A. *J. Neurochem.* **2007**, *102*, 712-722.
(31) Burmeister, J. J.; Palmer, M.; Gerhardt, G. A. *Biosens. Bioelectron.* **2005**, *20*, 1772-1779.
(32) Lourenço, C. F.; Ledo, A.; Laranjinha, J.; Gerhardt, G. A.; Barbosa, R. M. *Sens. Actuators, B* **2016**, *237*, 298-307.
(33) Burmeister, J. J.; Pomerleau, F.; Huettl, P.; Gash, C. R.; Werner, C. E.; Bruno, J. P.; Gerhardt, G. A. *Biosens. Bioelectron.* **2008**, *23*, 1382-1389.
(34) Parikh, V.; Pomerleau, F.; Huettl, P.; Gerhardt, G. A.; Sarter, M.; Bruno, J. P. *Eur. J. Neurosci.* **2004**, *20*, 1545-1554.
(35) Opris, I.; Fuqua, J. L.; Gerhardt, G. A.; Hampson, R. E.; Deadwyler, S. A. *J. Neurosci. Methods* **2015**, *244*, 104-113.
(36) Moxon, K. A.; Leiser, S. C.; Gerhardt, G. A.; Barbee, K. A.; Chapin, J. K. *IEEE Trans. Biomed. Eng.* **2004**, *51*, 647-656.
(37) Talauliker, P. M.; Price, D. A.; Burmeister, J. J.; Nagari, S.; Quintero, J. E.; Pomerleau, F.; Huettl, P.; Hastings, J. T.; Gerhardt, G. A. *J. Neurosci. Methods* **2011**, *198*, 222-229.
(38) Hascup, E. R.; af Bjerken, S.; Hascup, K. N.; Pomerleau, F.; Huettl, P.; Stromberg, I.; Gerhardt, G. A. *Brain Res.* **2009**, *1291*, 12-20.
(39) Sander, R. *Atmos. Chem. Phys.* **2015**, *15*, 4399-4981.
(40) Barbosa, R. M.; Lourenco, C. F.; Santos, R. M.; Pomerleau, F.; Huettl, P.; Gerhardt, G. A.; Laranjinha, J. *Methods Enzymol.* **2008**, *441*, 351-367.
(41) Burmeister, J. J.; Moxon, K.; Gerhardt, G. A. *Anal. Chem.* **2000**, *72*, 187-192.
(42) Burmeister, J. J.; Gerhardt, G. A. *Anal. Chem.* **2001**, *73*, 1037-1042.
(43) Franks, W.; Schenker, I.; Schmutz, P.; Hierlemann, A. *IEEE Trans. Biomed. Eng.* **2005**, *52*, 1295-1302.
(44) Han, J. H.; Boo, H.; Park, S.; Chung, T. D. *Electrochim. Acta* **2006**, *52*, 1788-1791.
(45) Brummer, S. B. *J. Phys. Chem.* **1965**, *69*, 562-&.
(46) Bett, J.; Kinoshit.K; Routsis, K.; Stonehar.P. *J. Catal.* **1973**, *29*, 160-168.
(47) Hai, B.; Tolmachev, Y. V.; Loparo, K. A.; Zanelli, C.; Scherson, D. *J. Electrochem. Soc.* **2011**, *158*, F15-F19.
(48) Amatore, C.; Pebay, C.; Thouin, L.; Wang, A. F. *Electrochem. Commun.* **2009**, *11*, 1269-1272.
(49) Bard, A. J.; Faulkner, L. R. *Electrochemical Methods, 2nd ed.*, 2nd ed.; Wiley: New York, 2000.
(50) Licht, S.; Cammarata, V.; Wrighton, M. S. *J. Phys. Chem.* **1990**, *94*, 6133-6140.
(51) Park, S.; Song, Y. J.; Boo, H.; Chung, T. D. *J. Phys. Chem. C* **2010**, *114*, 8721-8726.
(52) Venkatraman, S.; Hendricks, J.; King, Z. A.; Sereno, A. J.; Richardson-Burns, S.; Martin, D.; Carmena, J. M. *IEEE Trans. Neural Syst. Rehabil. Eng.* **2011**, *19*, 307-316.
(53) Chen, D.; Tao, Q.; Liao, L. W.; Liu, S. X.; Chen, Y. X.; Ye, S. *Electrocatalysis* **2011**, *2*, 207-219.
(54) Daubinger, P.; Kieninger, J.; Unmussig, T.; Urban, G. A. *Phys. Chem. Chem. Phys.* **2014**, *16*, 8392-8399.
(55) Inzelt, G.; Berkes, B. B.; Kriston, A. *Pure Appl. Chem.* **2011**, *83*, 269-279.
(56) Randles, J. E. B. *Discuss. Faraday Soc.* **1947**, *1*, 11-19.
(57) Cogan, S. F. *Annu. Rev. Biomed. Eng.* **2008**, *10*, 275-309.

(58) Robinson, D. A. *Proc. IEEE* **1968**, *56*, 1065-&.
(59) Jun, S. B.; Hynd, M. R.; Smith, K. L.; Song, J. K.; Turner, J. N.; Shain, W.; Kim, S. J. *Med. Biol. Eng. Comput.* **2007**, *45*, 1015-1021.
(60) Popke, H.; Mutoro, E.; Luerssen, B.; Janek, J. *J. Phys. Chem. C* **2012**, *116*, 1912-1920.
(61) Popke, H.; Mutoro, E.; Luerssen, B.; Janek, J. *Catal. Today* **2013**, *202*, 12-19.
(62) Weltin, A.; Slotwinski, K.; Kieninger, J.; Moser, I.; Jobst, G.; Wego, M.; Ehret, R.; Urban, G. A. *Lab Chip* **2014**, *14*, 138-146.
(63) Bazzu, G.; Puggioni, G. G.; Dedola, S.; Calia, G.; Rocchitta, G.; Migheli, R.; Desole, M. S.; Lowry, J. P.; O'Neill, R. D.; Serra, P. A. *Anal. Chem.* **2009**, *81*, 2235-2241.
(64) Bolger, F. B.; Bennett, R.; Lowry, J. P. *Analyst* **2011**, *136*, 4028-4035.
(65) Piilgaard, H.; Lauritzen, M. *J. Cereb. Blood Flow Metab.* **2009**, *29*, 1517-1527.
(66) Khennouf, L.; Gesslein, B.; Lind, B. L.; van den Maagdenberg, A. M.; Lauritzen, M. *Ann. Neurol.* **2016**, *80*, 219-232.
(67) Jessen, S. B.; Brazhe, A.; Lind, B. L.; Mathiesen, C.; Thomsen, K.; Jensen, K.; Lauritzen, M. *Cereb. Cortex* **2015**, *25*, 2594-2609.
(68) Ledo, A.; Barbosa, R. M.; Gerhardt, G. A.; Cadenas, E.; Laranjinha, J. *Proc. Natl. Acad. Sci. U. S. A.* **2005**, *102*, 17483-17488.
(69) Ledo, A.; Barbosa, R.; Cadenas, E.; Laranjinha, J. *Free Radic. Biol. Med.* **2010**, *48*, 1044-1050.
(70) Xiang, L.; Yu, P.; Zhang, M.; Hao, J.; Wang, Y.; Zhu, L.; Dai, L.; Mao, L. *Anal. Chem.* **2014**, *86*, 5017-5023.
(71) Miller, E. M.; Quintero, J. E.; Pomerleau, F.; Huettl, P.; Gerhardt, G. A.; Glaser, P. E. *J. Neurosci. Methods* **2015**, *252*, 75-79.

**For TOC Only**

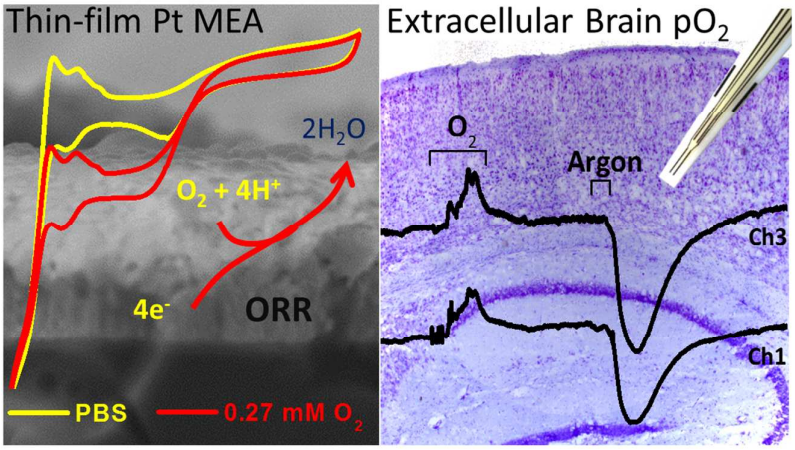
Thin-film Pt MEA
2H2O
O2 + 4H+
4e-
ORR
PBS
0.27 mM O2
Extracellular Brain pO2
O2
Argon
Ch3
Ch1

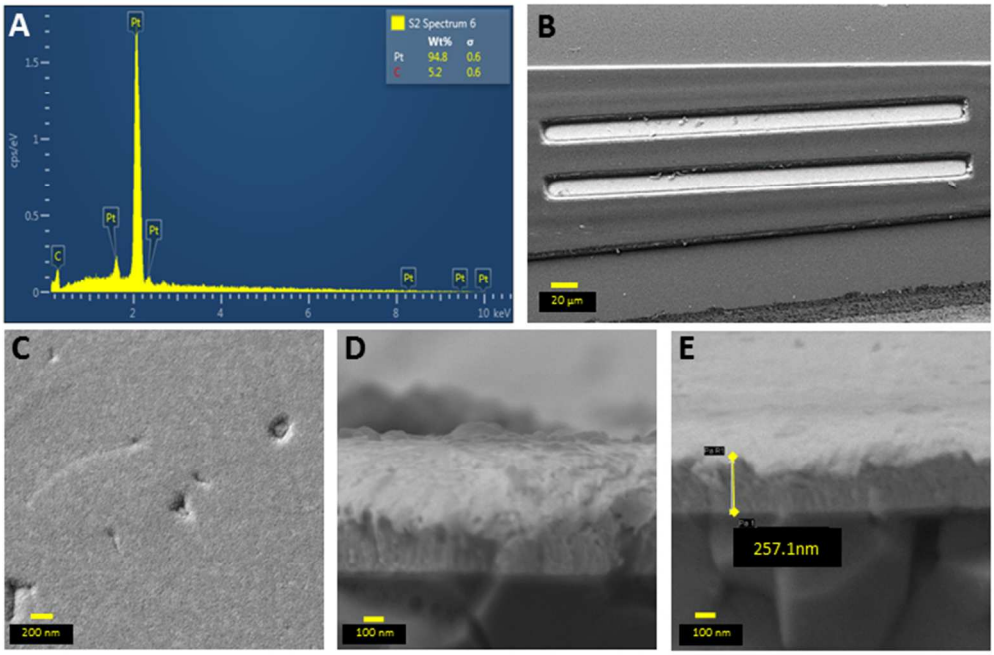


Figure 1 – Morphological and chemical analysis of the ceramic-based MEA Pt surface. A) Elemental composition of a Pt site of the S2 MEA obtained by SEM/EDX elemental analysis at 10 keV. B) SEM micrograph image of the top pair of Pt sites at the MEA tip, showing the polyimide insulation layer and the ceramic subtract and C) high magnification view of the smooth Pt surface. D) Cross-section SEM micrographs of the Pt layer over the ceramic substrate wafer showing nano-size elevations of Pt surface and E) the reduced thickness of the thin Pt film.

Fig. 1

200x131mm (96 x 96 DPI)

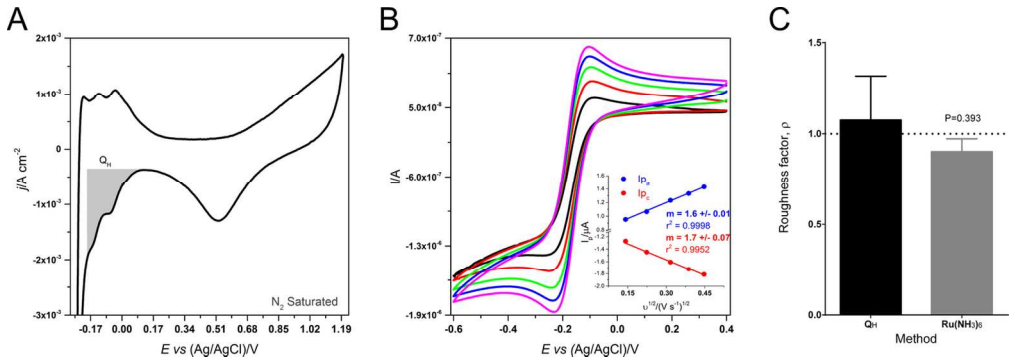


Figure 2 - Determination of the electrochemically active surface area (ECSA) of the Pt sites on the MEAs. A) Representative cyclic voltammogram (25$^{th}$ scan) in $N_2$ saturated 0.5 M $H_2SO_4$ of a Pt MEA surface. Shaded area (QH) represents section used to determine the hydrogen adsorption ($H_{upd}$) charge. B) Cyclic voltammograms recorded in 5.0 mM $Ru(III)(NH_3)_6$ in 0.5 M KCl at scan rates (υ) of 25, 50, 100, 150 and 200 mV $s^{-1}$ for a Pt surface and the inset is the plot of anodic (Ipa) and cathodic (Ipc) peak currents as a function of $u^{1/2}$ showing the respective slope (m) ± SE. C) The bar graph shows the mean roughness factor (ρ) of the Pt sites determined by each method. Values represent mean ± SD. Dashed line highlights ρ=1, where the ECSA equals the geometric area.

Fig. 2

136x47mm (300 x 300 DPI)

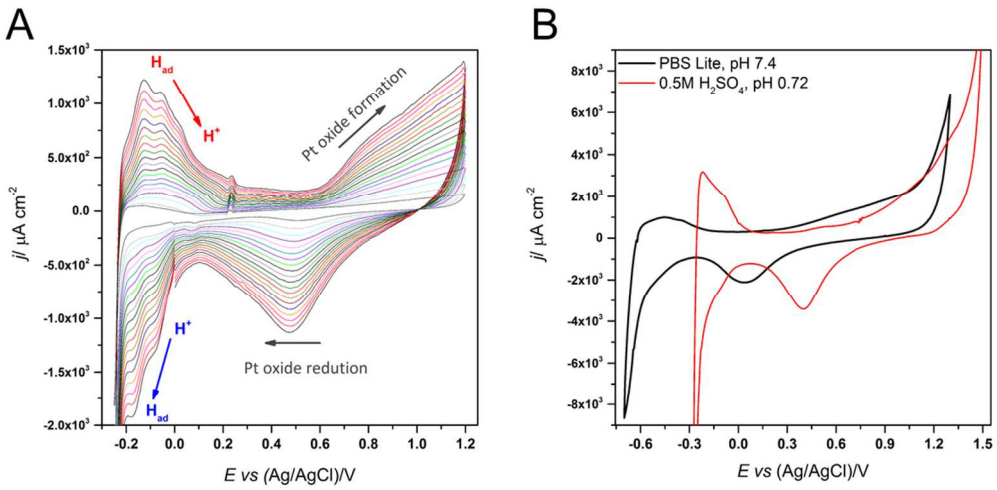


Figure 3 – Electrochemical behavior in acidic and neutral electrolyte media. A) Successive cyclic voltammograms (25$^{th}$ scan) at increasing scan rates (50-1000 mV $s^{-1}$) obtained in $N_2$ saturated 0.5 M $H_2SO_4$, detailing the typical Pt oxide formation and reduction, proton adsorption (2 peaks) and reduction (3 peaks) and double layer zones. B) Comparative CV plots (0.2 V $s^{-1}$) recorded in $N_2$-saturated 0.05 M PBS, pH 7.4 (black line) and $N_2$-saturated 0.5 M $H_2SO_4$, pH 0.72 (red line) highlighting the positive shift in hydrogen evolution potential and increasing currents for Pt-oxide formation and reduction at lower pH on the Pt surface of the MEAs.

Fig. 3

99x49mm (300 x 300 DPI)

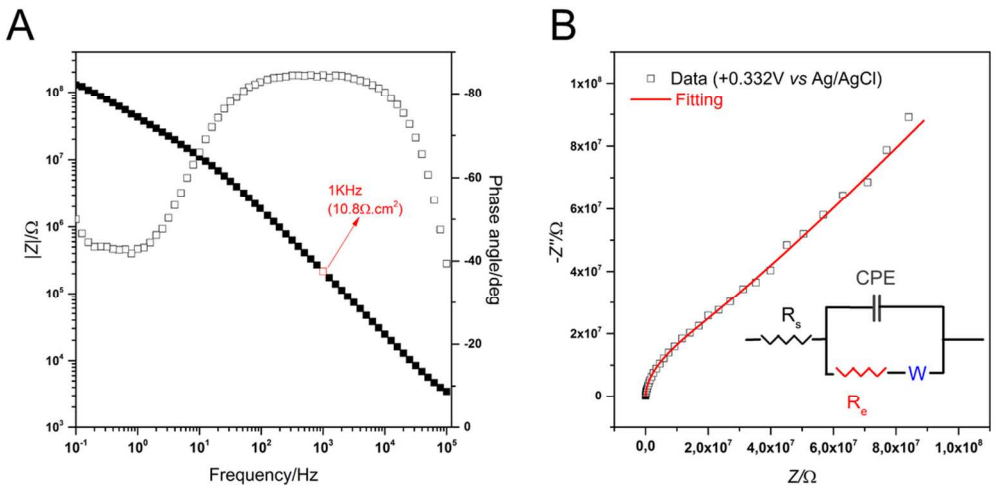


Figure 4 – Electrochemical impedance spectroscopy measurements. A) Impedance-frequency plot (Bode plot) at the open circuit potential (OCP) of +0.332V *vs* Ag/AgCl of an MEA Pt site. Filled squares represent |Z| values and open squares are those obtained for the phase shift. The open red square highlights the |Z| value at 1 kHz. B) Complex plane electrochemical impedance spectrum (Nyquist plot) of experimental data (open squares) for the MEAs. Red line shows fitting to the electrical equivalent circuit shown in the inset. $R_s$ solution resistance, $R_e$ electron or charge transfer resistance, W Warburg impedance element, and CPE constant phase element.

Fig. 4

99x49mm (300 x 300 DPI)

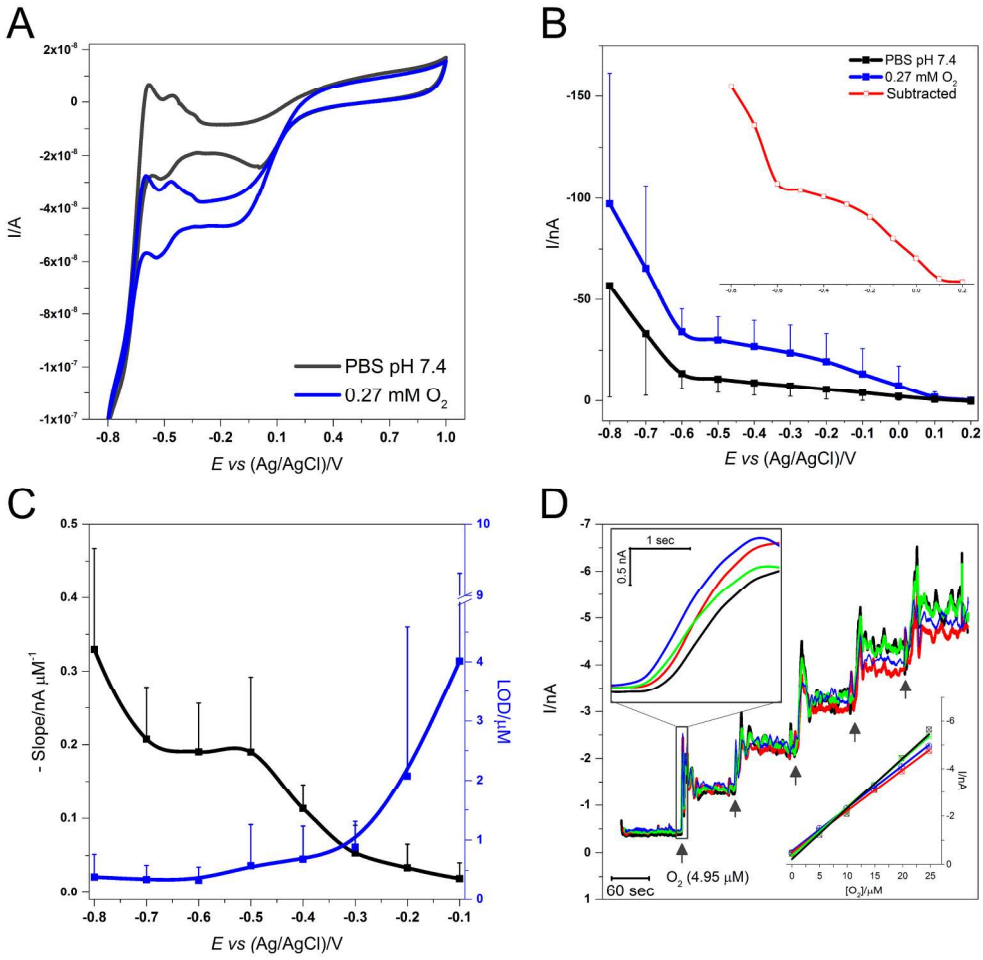


Figure 5 – Electrochemical behavior of oxygen reduction at the Pt MEA surface. A) Cyclic voltammograms recorded at 100 mV $s^{-1}$ and B) amperometric current as a function of the applied potential in PBS in the absence ($N_2$ saturated) (grey line) and presence of $O_2$ (blue line) (air-saturated) in the solution. The inset in B) displays the subtracted current response. C) Sensitivity and LOD data obtained at different reduction potentials at 37 ºC for the Pt surface of the MEA. D). Plot shows a representative 4-channel calibration obtained at -0.6 V *vs* Ag/AgCl and the calibration curve for each channel (inset) of an MEA. Highlighted in the top left corner is the response of the 4 channels to the first addition of $O_2$ solution, showing fast response despite slow stirring of solution. Data in B) and C) represent mean ± SD. The SD bars are presented only in one direction for graphical simplicity.

Fig. 5
199x199mm (300 x 300 DPI)

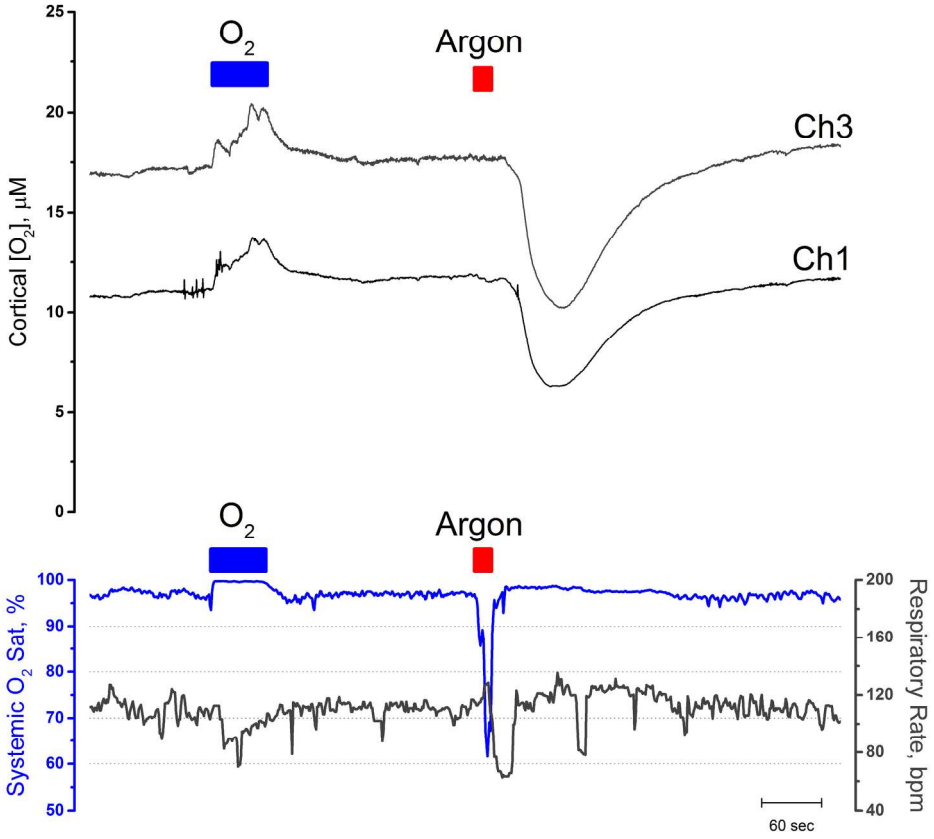


Figure 6 – Oxygen measurement *in vivo* in the brain of an anesthetized rat. Amperometric recording obtained from a MEA implanted in the rat cerebral cortex. Increase and decrease in local $pO_2$ as a result of having the animal breath $O_2$ saturated air (blue box) or Ar saturated air (red box). Top panel shows amperometric response from 2 sites while the lower panel shows changes in systemic $O_2$ saturation (blue line) and breath rate (grey line).

Fig. 6

199x199mm (300 x 300 DPI)